J. Fluid Mech. (2020), *vol.* 885, A32. © Cambridge University Press 2019
doi:10.1017/jfm.2019.995

Analysis of premixed flame kernel/turbulence interactions under engine conditions based on direct numerical simulation data

T. Falkenstein[1], S. Kang[2] and H. Pitsch[1,†]

[1]Institute for Combustion Technology, RWTH Aachen University, 52056 Aachen, Germany

[2]Department of Mechanical Engineering, Sogang University, Seoul 121-742, Republic of Korea

(Received 31 March 2019; revised 27 August 2019; accepted 22 November 2019)

Although the evolution of premixed flames in turbulence has been frequently studied, it is not well understood how small flames interact with large-scale turbulent flow motion. Since this question is of practical importance for the occurrence of cycle-to-cycle variations in spark ignition engines, the objective of the present work is to fundamentally differentiate early flame kernel development from well-established turbulent flame configurations. For this purpose, a direct numerical simulation database consisting of three flames propagating in homogeneous isotropic turbulence (Falkenstein *et al.*, *Combust. Flame*, 2019, Preprint, arXiv:1908.07556 (accepted)) is considered. The flames feature different ratios of the initially laminar flame diameter to the integral length scale. To quantify flame kernel development, the time evolution of flame topology and flame front geometry are analysed in detail. It is shown that some realizations of the early flame kernel are substantially influenced by high compressive strain caused by large-scale turbulent flow motion with characteristic length scales greater than the flame kernel size. As a result, the initial spherical kernel topology may become highly distorted, which is reflected in the stochastic occurrence of excessive curvature variance. Two mechanisms of curvature production resulting from early flame kernel/turbulence interactions are identified by analysis of the mean curvature balance equation. Further, it is shown that the curvature distribution of small flame kernels becomes strongly skewed towards positive curvatures, which is contrary to developed turbulent flames. Hence, the transition of ignition kernels to self-sustaining turbulent flames is very different in nature compared with the development of a statistically planar flame brush.

Key words: combustion, flames, turbulent reacting flows

1. Introduction

The development and control of clean and efficient technical combustion devices is often very challenging due to the potential occurrence of undesirable stochastic phenomena. In spark ignition (SI) engines, efforts to enhance thermal efficiency by lean or exhaust-gas-diluted operation are limited by reduced combustion stability

† Email address for correspondence: office@itv.rwth-aachen.de

https://doi.org/10.1017/jfm.2019.995 Published online by Cambridge University Press

(Aleiferis *et al.* 2004; Jung, Sasaki & Iida 2017). In extreme cases, partially burning or misfiring cycles may occur (Peterson, Reuss & Sick 2011) leading to poor efficiency and excessive emissions. At high-load conditions, cycle-to-cycle variations (CCV) may necessitate significant safety margins to avoid potentially destructive irregular combustion phenomena, such as knock (Wang, Liu & Reitz 2017).

From experimental engine studies, it is well-known that CCV are correlated with fluctuations in early flame kernel development (Young 1981). Even under conditions that lead to misfires, spark ignition was found to successfully initiate a flame kernel, which extinguishes during the early growth phase (Peterson *et al.* 2011). By using advanced optical diagnostics, prolonged chemical time scales due to exposure of the small flame to a locally lean or diluted mixture (Peterson, Reuss & Sick 2014), or fluctuations in large-scale flow structures (Bode *et al.* 2017; Zeng *et al.* 2019) and kinetic energy (Buschbeck *et al.* 2012) could be identified as sources for cyclic variability. Schiffmann, Reuss & Sick (2018) have shown that the time until the young laminar flame kernel transitions to a turbulent flame correlates with CCV.

A particular feature of the combustion process in conventional SI engines is flame initiation at unfavourably small length scales in terms of resilient flame growth, mainly for three reasons. First, the radius of the young flame kernel is only moderately larger than the flame thickness, which may severely alter the flame structure as well as the reaction/diffusion balance therein. Second, large portions of the initially small burned-gas volume may be in contact with colder walls, thus causing significant heat losses. Third, the flame kernel is initially smaller than the energetic flow scales, which may have several implications. As observed in fundamental experiments by Akindele *et al.* (1982) and Bradley & Lung (1987), the young flame kernel can be subject to convective transport attributed to flow structures with larger characteristic length scales than the kernel size, before the onset of noticeable flame wrinkling by turbulence. Further, it was hypothesized that the early turbulent flame growth is governed by the high-wavenumber range of the energy spectrum, while lower wavenumbers were thought to be mostly inactive during early flame front/turbulence interactions (Akindele *et al.* 1982; Abdel-Gayed, Al-Khishali & Bradley 1984). This concept of scale separation based on the characteristic flame kernel size as upper cutoff scale was also introduced into models (Herweg & Maly 1992; Echekki *et al.* 1994), which were proposed as extensions to previous expressions for turbulent flame brush development (Scurlock & Grover 1953; Meneveau & Poinsot 1991). However, the additional effect of flame kernel stretching by hydrodynamic strain mentioned by Bradley *et al.* (1994) has not received much attention and is considered in the present direct numerical simulation (DNS) study.

For a quantitative analysis of turbulent premixed flame development, different metrics, such as flame area or flame curvature, may be considered, which will be briefly introduced hereafter. The global flame front geometry can be characterized by the flame brush thickness or flame surface area (Peters 1999), which is directly related to the increase in the overall burning rate due to turbulence (Damköhler 1940). Candel & Poinsot (1990) derived a balance equation for the flame area, here defined as an iso-surface of a scalar ϑ propagating with the displacement speed s_d

$$\frac{1}{A_\vartheta}\frac{\mathrm{D}_\vartheta(A_\vartheta)}{\mathrm{D}_\vartheta(t)} = a_t^{(\vartheta)} + s_d^{(\vartheta)}\kappa^{(\vartheta)}. \tag{1.1}$$

According to (1.1), flame area may change due to hydrodynamic strain expressed by the tangential strain rate a_t, and the propagation of surface elements with local mean

https://doi.org/10.1017/jfm.2019.995 Published online by Cambridge University Press

curvature

$$\kappa^{(\vartheta)} = \frac{\partial n_i^{(\vartheta)}}{\partial x_i}, \tag{1.2}$$

$$n_i^{(\vartheta)} = \frac{-1}{|\nabla \vartheta|} \frac{\partial \vartheta}{\partial x_i}. \tag{1.3}$$

Note that the sub/superscripts indicating the scalar field will be omitted in most parts of the present discussion. The total time derivative in a reference frame attached to the propagating scalar iso-surface is defined as:

$$\frac{\mathrm{D}_\vartheta(\cdot)}{\mathrm{D}_\vartheta(t)} = \frac{\partial(\cdot)}{\partial t} + (u_i + s_d^{(\vartheta)} n_i^{(\vartheta)}) \frac{\partial(\cdot)}{\partial x_i}, \tag{1.4}$$

where u_i denotes the fluid velocity and n_i is the normal vector pointing into the direction of negative scalar gradient. For $(\cdot) = (\vartheta)$, the left-hand side of (1.4) vanishes, which can be used to determine s_d.

Flame curvature is a useful quantity to parametrize variations in local flame structure (Kim & Pitsch 2007), and to statistically assess the flame front geometry in turbulence. To highlight the connection between total flame area and the first two moments of the curvature probability density function (PDF), the integral form of (1.1), can be used to express the evolution of the total flame surface area inside the volumetric domain Ω

$$\frac{1}{\overline{A}_\Omega} \frac{\mathrm{D}_\vartheta(\overline{A}_\Omega)}{\mathrm{D}_\vartheta(t)} = \langle a_t \rangle_{s,\Omega} + \langle s_d \kappa \rangle_{s,\Omega}, \tag{1.5}$$

$$= \langle a_t \rangle_{s,\Omega} + \langle s_{rn} \kappa \rangle_{s,\Omega} - \langle D_{th} \kappa^2 \rangle_{s,\Omega}. \tag{1.6}$$

Here, $\langle \cdot \rangle_s$ denotes generalized surface averaging as proposed by Boger *et al.* (1998), i.e. the averaging operation is defined by computing the surface integral of some quantity over each scalar iso-surface, averaging over all iso-levels and normalizing by the averaged scalar iso-surface area $\overline{A}_\Omega = \int_\Omega |\nabla \vartheta| \, \mathrm{d}V$. Further, the displacement speed has been decomposed into contributions by reaction/normal diffusion (s_{rn}) and tangential diffusion ($-D_{th}\kappa$) according to Echekki & Chen (1999), where D_{th} is the thermal diffusivity. Hence, the second term on the right-hand side of (1.6) describes the total area change due to normal propagation of curved flame regions (kinematic restoration, which could be a source or sink for flame area depending on the sign of the curvature), while the third term corresponds to scalar dissipation (Peters 1999). The impact of curvature moments on global flame area dynamics can be shown by adapting the decomposition of $\langle s_d \kappa \rangle_{s,\Omega}$ proposed by Wang *et al.* (2017) to the normal propagation and scalar dissipation terms in (1.6)

$$\langle s_{rn} \kappa \rangle_s = \langle s_{rn} \rangle_s \langle \kappa \rangle_s + [\langle s_{rn} \kappa \rangle_s - \langle s_{rn} \rangle_s \langle \kappa \rangle_s], \tag{1.7}$$

$$-\langle D_{th} \kappa^2 \rangle_s = -\langle D_{th} \rangle_s \langle \kappa^2 \rangle_s - [\langle D_{th} \kappa^2 \rangle_s - \langle D_{th} \rangle_s \langle \kappa^2 \rangle_s], \tag{1.8}$$

where the subscript Ω has been omitted for brevity. Wang *et al.* (2017) have shown that the correlation of curvature and displacement speed dominates the overall curvature stretch effect $\langle s_d \kappa \rangle_s$ in (1.5). However, separating the curvature effect on flame area evolution into normal propagation and scalar dissipation enables a more differentiated understanding. Although the correlation between curvature and the flame

https://doi.org/10.1017/jfm.2019.995 Published online by Cambridge University Press

normal propagation velocity in (1.7) may only be negligible in the unity-Lewis-number limit and if the flame is fully developed, the contribution of $\langle s_{rn}\kappa\rangle_s$ to the global curvature stretch term $\langle s_d\kappa\rangle_s$ is small under the present conditions (cf. figure S-1(*b*) in the supplementary material available at https://doi.org/10.1017/jfm.2019.995). While the scalar dissipation term is of leading order, the correlation between the thermal diffusivity and the squared curvature in (1.8) is rather weak and may be neglected (cf. figure S-1(*c*) in the supplementary material). Hence, the following approximations are introduced:

$$\langle s_{rn}\kappa\rangle_s \approx \langle s_{rn}\rangle_s\langle\kappa\rangle_s, \tag{1.9}$$

$$-\langle D_{th}\kappa^2\rangle_s \approx -\langle D_{th}\rangle_s\langle\kappa^2\rangle_s. \tag{1.10}$$

To relate the evolution of total flame surface area to the surface-weighted curvature PDF, (1.9) and (1.10) are inserted into (1.6) and rewritten in terms of the first two central curvature moments $\mu_\kappa = \langle\kappa\rangle_s$ and $\sigma_\kappa^2 = \langle\kappa^2\rangle_s - \mu_\kappa^2$,

$$\frac{1}{\overline{A}_\Omega}\frac{\mathrm{D}_\vartheta(\overline{A}_\Omega)}{\mathrm{D}_\vartheta(t)} \approx \langle a_t\rangle_s + [\langle s_m\rangle_s - \langle D_{th}\rangle_s\mu_\kappa]\mu_\kappa - \langle D_{th}\rangle_s\sigma_\kappa^2. \tag{1.11}$$

It should be noted that the theoretical analysis by Peters (1999) identified the scalar dissipation term in (1.6), i.e. the impact of σ_κ^2 on the total flame area (cf. (1.11)), as the dominant curvature term in the thin reaction zones regime. In empirical studies, the effect of increasing turbulence intensity u'/s_l^0 on flame wrinkling was quantified by means of flame surface area (Wenzel & Peters 2000) and in terms of σ_κ^2 as the most informative curvature moment in terms of flame front/turbulence interactions (Haq *et al.* 2002; Shepherd *et al.* 2002; Gashi *et al.* 2005).

In our previous study (Falkenstein *et al.* 2019), a DNS database of three developing turbulent premixed flames has been established in the limit of unity Lewis number. It was shown that the global heat release rate of small flame kernels exhibits run-to-run variations, which were attributed to stochastic variations in surface area evolution caused by the dissipation term in (1.6). However, the fundamental role of turbulence in shaping the young flame kernel has not been clarified. In this study, the particular nature of flame kernel development will be analysed in terms of the evolution of central curvature moments, which are related to flame area dynamics according to (1.11). The occurrence of excessive curvature variance and positive curvature skewness during the early phase of small flame kernel growth will be explained by evaluation of the flame curvature balance equation. Further, the role of large-scale turbulent flow structures in changing the small flame kernel topology will be shown.

The present manuscript is organized as follows. In § 2, a brief summary of the DNS database is given. Characteristic differences in the flame topologies of small flame kernels and developing spherical flames are presented in § 3. A detailed analysis of flame front geometry evolution in terms of mean curvature dynamics is provided in § 4. Length-scale-dependent flame front alignment with the flow field is the subject of § 5. Finally, the relevance of the present results to actual engines and implications for modelling of early flame kernel development are discussed in § 6.

2. DNS database

To isolate the governing physical phenomena stemming from the small initial flame size characteristic for SI engine combustion, a DNS database consisting of three flame configurations with different geometries and multiple realizations for the most relevant case (Falkenstein *et al.* 2019) is considered. A summary of the parameter variations, flame conditions and the DNS set-up is provided in the following sections.

https://doi.org/10.1017/jfm.2019.995 Published online by Cambridge University Press

2.1. *Flame geometry variation*

A few studies in the literature have proposed regime diagrams for flame kernel/flow interactions derived from two-dimensional DNS data of laminar (Echekki & Kolera-Gokula 2007; Vasudeo *et al.* 2010) or turbulent (Reddy & Abraham 2013) flames. Two governing parameters were identified, the ratio of integral length scale (or vortex size) to kernel size, as well as the ratio of turbulent velocity fluctuation (or vortex strength) to burning velocity. While these studies established a qualitative understanding of global flame kernel/flow interactions, quantitative differences between identified regimes and consequences for the developed flames were not reported. In this work, we seek to gain quantitative insight into early flame kernel development under engine conditions by means of three-dimensional DNS with detailed chemistry. Here, we will focus on variations of the ratio of initial flame diameter D_0 to the integral length scale l_t, while the ratio of velocity fluctuation to burning velocity u'/s_l^0 is kept constant. The main reference case here is the engine flame kernel with $D_0/l_t = 0.3$, which was computed in a constant volume setting. For this case, the choice of the initial diameter is not unique since ignition and early flame development cannot be clearly distinguished in real engines. Justification for the selected parameter value will be provided in § 6. Since the global flame kernel behaviour for $D_0/l_t = 0.3$ depends particularly strongly on the local flow conditions, two kernel realizations have been obtained by igniting the kernel in different locations of the same initial flow field. The second considered case is a larger flame kernel dataset that has been designed with $D_0/l_t = 2.0$ such that the initial flame kernel is larger than the integral scale of the turbulence, i.e. the initial interaction of the flame kernel with the turbulence is fundamentally different from that of the engine flame kernel. Finally, since both of these flame kernels have mean positive curvature, an initially laminar, planar flame front propagating in homogeneous isotropic turbulence is also considered as a well-defined, limiting reference case with $D_0/l_t = \infty$, which was computed in a constant pressure setting. Here, all flow scales contribute to flame corrugation from the beginning. Additionally, D_0/l_t does not change over time. For illustrations of the flames, refer to a previous study by the present authors (Falkenstein *et al.* 2019).

2.2. *Physical configuration*

Mixture state and composition have been chosen to be representative of fully homogeneous, stoichiometric SI engine operation at low load. To enable a better understanding of how the flow alters the young flame kernel, Lewis numbers (Le) of all species have been artificially set to unity. Flame response in presence of differential diffusion will be investigated in a future study. Mixture properties of the DNS are summarized in table 1. The thermodynamic state is given by the pressure $p^{(0)}$ and temperature of the unburned gas T_u, which has unity equivalence ratio ϕ. In order to provide well defined but engine-relevant flow configurations, all flames have been computed in decaying homogeneous isotropic turbulence (h.i.t.). A comparison between engine and DNS parameters is summarized in table 2. The turbulent integral length scale and eddy turnover time are denoted by l_t and τ_t, and η is the Kolmogorov length scale. In this study, the laminar flame thickness l_f is computed from the maximum temperature gradient, while a turbulent length scale representative of the integral scales is given by $l_t = u'^3/\overline{\varepsilon}$, using the mean dissipation rate $\overline{\varepsilon}$. Except for the integral length scale of turbulence, which is approximately 2.5 times smaller than in a practical engine, the conditions are realistic for the full duration of the DNS.

https://doi.org/10.1017/jfm.2019.995 Published online by Cambridge University Press

Mixture	Iso-octane/air
$p^{(0)}$	6 bar
T_u	600 K
ϕ	1.0
s_l^0	0.63 m s^{-1}
l_f	71.3 µm
Le	1.0
Flow field	Decaying h.i.t.
Combust. regime	Thin rct. zones

TABLE 1. Flame conditions in the DNS.

Parameter	Engine	DNS ($t_{init} - t_{end}$)
Re_t	100–2390	385–222
$\frac{u_{rms}}{s_l^0}$	2–15	7.0–3.1
Ka	1–6	13.7–4.2
Da	1–100	1.4–3.6
$\frac{l_t}{\eta}$	100–200	87.2–57.2
$\frac{l_t}{l_f}$	20–147	10.2–12.4
$\frac{D_0}{l_t}$	<1.0	$0.3 \mid 2.0 \mid \infty$

TABLE 2. Engine (Heywood 1994; Heim & Ghandhi 2011) and DNS characteristic numbers.

More details on the flow field initialization and non-reactive DNS results are provided in our previous study (Falkenstein *et al.* 2019).

A summary of the DNS set-up is provided in table 3. One important difference between the flame kernel datasets and the planar reference flame is the initialization method. Flame kernels were ignited by a source term in the temperature equation with similar spark duration and size as previously used in the literature (Hesse, Chakraborty & Mastorakos 2009; Subramanian, Domingo & Vervisch 2009; Uranakara, Chaudhuri & Lakshmisha 2017). To reliably ignite flame kernels under turbulent conditions, a 40 % higher ignition energy than the minimum ignition energy (MIE) of a laminar flame was used, which results in an early growth phase comparable to engine experiments reported in the literature (cf. § 6). By contrast, a laminar unstretched flame was imposed into the turbulent flow field as initial condition for the planar flame DNS to avoid strong dilatation due to the larger burned volume.

3. Flame kernel topology evolution

In fully developed turbulent flames, the flame brush thickness is proportional to the integral length scale (Peters 1992). However, during early flame kernel development in engines, the size of the flame kernel is typically smaller or of the same order as the energy-containing flow scales. Accordingly, some models for early flame

https://doi.org/10.1017/jfm.2019.995 Published online by Cambridge University Press

Grid size	960^3
Domain size	$15 \cdot l_t$
$l_f/\Delta x$; $\eta/\Delta x$	6 (Luca *et al.* 2019); 0.7
Navier–Stokes eq.	Low Mach approx. (Müller 1998)
Transport model	(Hirschfelder, Curtiss & Bird 1954), const.-*Le*
Soret effect	Yes
Chem. mechanism	26 Spec., based on (Pitsch & Peters 1996)
Flame kernel init.	Ignition heat source
Sim. time of flame kernel realizations	Engine kernel I: $(t_{sim.} = 2.3 \cdot \tau_t)$, Engine kernel II: $(t_{sim.} = 1.0 \cdot \tau_t)$

TABLE 3. Computational set-up of the DNS.

kernel development are based on the idea that only flow scales smaller than the flame size contribute to early flame kernel area production through surface wrinkling (Herweg & Maly 1992; Echekki *et al.* 1994). In figure 1, flame front segments of one engine-relevant flame kernel realization and of the large flame kernel are shown at two time instants during early flame development. The comparison of both volumetric flame topologies indicates that the engine-relevant flame kernel significantly deviates from a wrinkled spherical flame, which will be quantified in § 3.1. While the flame surface of the large flame kernel becomes successively wrinkled by turbulence, the small kernel exhibits only moderate deviations from the flame mean curvature in most parts, but features some regions with excessive positive curvature. Hence, the curvature distribution as a measure for the flame front geometry can be expected to differ substantially between both flames, which will be investigated in § 4. Additionally, figure 1(*a*,*b*) suggests that the flame front normal orientation of the engine-relevant kernel is preferentially aligned with the most compressive principal strain vectors and that high-strain regions tend to form flat nibs. To identify the role of large-scale flow structures in shaping the young flame, the length-scale dependence of flame front/strain alignment statistics will be analysed in § 5.

3.1. *Early flame kernel deformation*

Figure 1 shows that the topology of the engine kernel is quite different from that of the larger kernel. This will be discussed based on quantitative measures in this section. Qualitative regime diagrams which characterize flame kernel/flow interactions based on a velocity- and a length-scale ratio (Echekki & Kolera-Gokula 2007; Vasudeo *et al.* 2010; Reddy & Abraham 2013) distinguish between kernel wrinkling and kernel breakthrough or breakup behaviour. In the latter regime, high straining flow motion leads to a global distortion of the small flame and eventually generates spatially separated regions of burned mixture, possibly resulting in local extinction. In the present engine-relevant DNS datasets, the flame kernels maintain a coherent flame surface at all times. Still, the early flame/turbulence interaction significantly differs from the large flame kernel, as will be shown below.

To track flame topology changes, Echekki & Kolera-Gokula (2007) used flame length as a parameter in a study on two-dimensional laminar vortex/flame kernel interactions. In cases which were attributed to the kernel breakthrough regime, interactions on the product side between the leading and the trailing edges of the highly distorted flame fronts were identified. In this work, the local thickness $d_{f,n}$ of the burned-gas region enclosed by a temperature iso-surface is used to parameterize

https://doi.org/10.1017/jfm.2019.995 Published online by Cambridge University Press

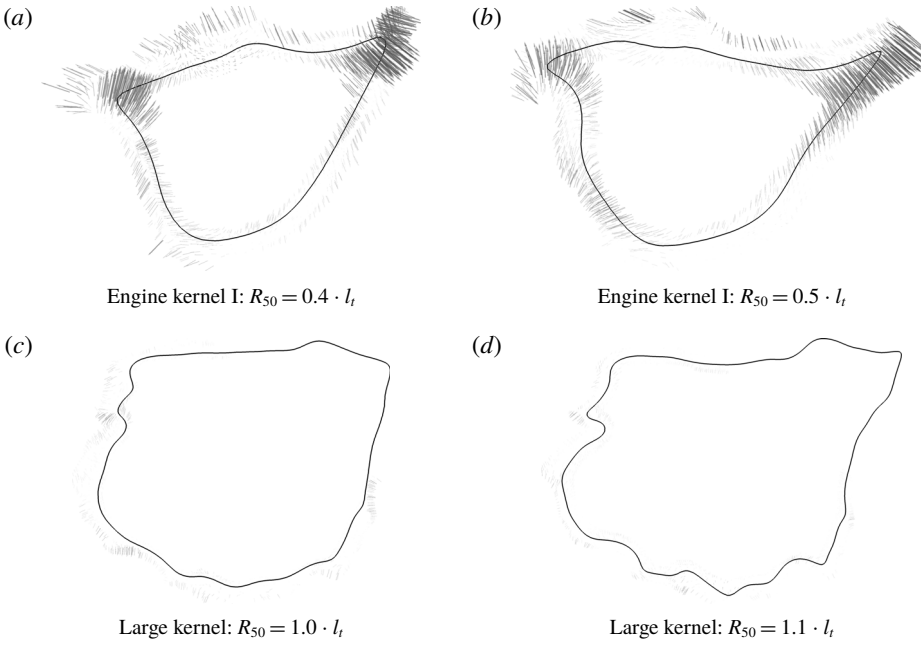


FIGURE 1. Temperature iso-contours and eigenvectors of the most compressive strain of engine flame kernel I (*a*,*b*), and of the large flame kernel plotted at reduced scale (*c*,*d*) at $(t = 0.17 \cdot \tau_t)$ and $(t = 0.25 \cdot \tau_t)$, respectively.



FIGURE 2. Definition of the burned region thickness $d_{f,n}$.

the volumetric flame topology. At every surface point, $d_{f,n}$ is determined by launching a ray into the opposite direction of the local normal vector and computing the distance to the closest intersection with the iso-surface on the opposite side of the flame. Hence, $d_{f,n}$ characterizes the distance between the leading and the trailing edge of two flame segments on either side of the flame kernel. An illustration is provided in figure 2. To obtain a flame topology measure that takes into account the flame kernel size and is not affected by the choice of the temperature iso-surface, $d_{f,n}$ has been normalized by the equivalent diameter D_v of a sphere with the same burned volume as enclosed by the iso-surface.

The PDFs of $d_{f,n}/D_v$ shown in figure 3 have been computed from 13 temperature iso-surfaces across the reaction zone of each flame and are considered as a measure for the overall flame shape. For a perfect sphere, one would obtain a delta function at unity. Close to the flame kernel breakthrough regime, a significant portion of the flame is expected to feature small distances between the leading and the trailing edges.

https://doi.org/10.1017/jfm.2019.995 Published online by Cambridge University Press

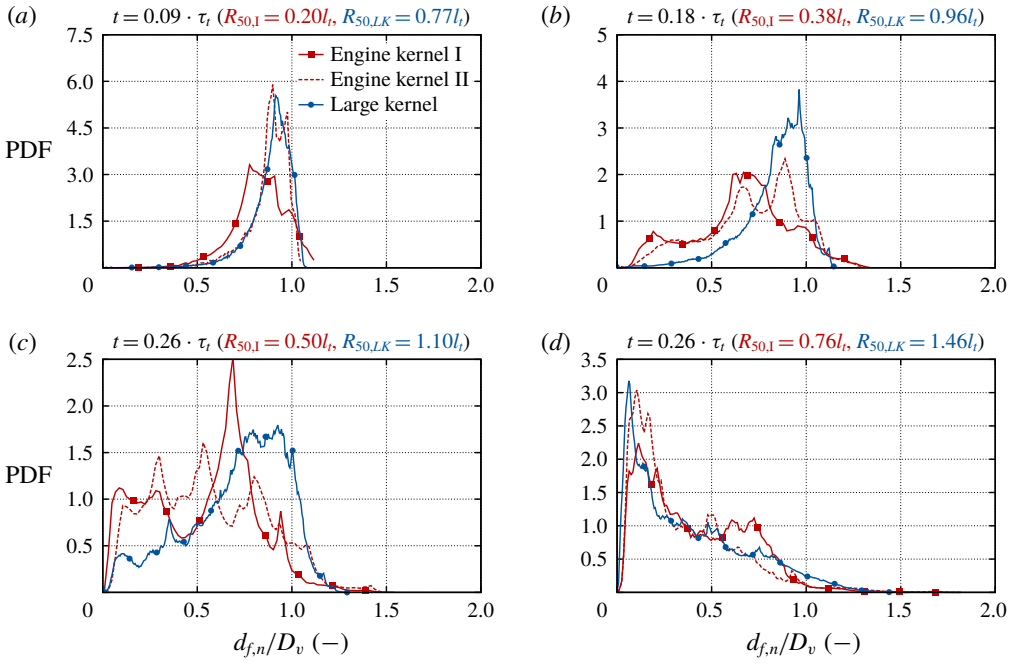


FIGURE 3. PDFs of normalized burned region thickness at different times. D_v is the diameter of a sphere with the same burned volume as the actual flame. (*a*) $t = 0.09 \cdot \tau_t$, (*b*) $t = 0.18 \cdot \tau_t$, (*c*) $t = 0.26 \cdot \tau_t$ and (*d*) $t = 0.53 \cdot \tau_t$.

For investigations on kernel extinction, normalization by the laminar flame thickness might be more suitable.

As can be seen in the figure, the geometry of all three flame kernels is initially determined by the ignition heat source. However, the PDFs develop very differently. While the large flame kernel maintains its overall shape during early flame growth, the small kernels quickly develop very thin geometric patterns with higher statistical significance. This is clearly visible during ($t = 0.18..0.26 \cdot \tau_t$), when the overall multimodal distributions of $d_{f,n}/D_v$ indicate distorted engine flame kernel topologies, which significantly deviate from spherical shape. By contrast, wrinkling of the large flame kernel by turbulent eddies slowly develops thin flame structures ('fingers'). This rather gradual process is indicated by the long monotonic tail of the PDF at ($t = 0.18 \cdot \tau_t$). Flame front corrugation by turbulence eventually causes a high probability of thin structures, while distances $d_{f,n}$ of the order of the equivalent flame diameter D_v become rather unlikely. In fact, the PDFs of all three flame kernels approach a similar distribution at ($t = 0.53 \cdot \tau_t$). This indicates that the different nature of early turbulent flame kernel development depending on the length-scale ratio D_0/l_t is restricted to the very initial phase. With respect to differences between both engine-relevant flame kernel realizations, engine kernel I is initially subject to stronger deformation (cf. figure 3*a*) caused by large-scale turbulent flow structures, as will be shown in § 5. While turbulence rapidly generates small geometric length scales in similar portions of the flame kernels during ($t = 0.18..0.26 \cdot \tau_t$), noticeable differences between both realizations are shown at larger $d_{f,n}/D_v$. The gradual disappearance of local maxima of the order of at least the equivalent flame radius may be interpreted as a measure for the transition to a fully developed turbulent flame.

https://doi.org/10.1017/jfm.2019.995 Published online by Cambridge University Press

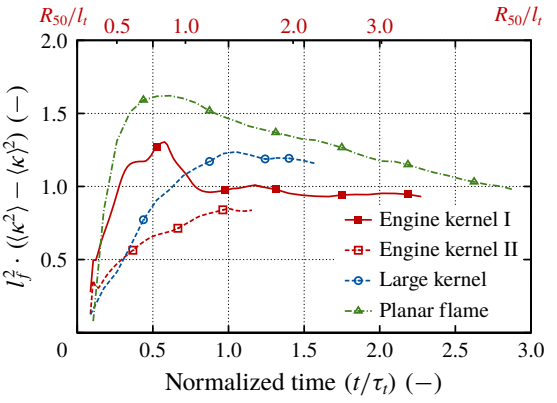


FIGURE 4. Evolution of the curvature variance for all flames. The upper x-axis indicates the size of engine kernel I.

4. Flame front geometry evolution

In the previous section, it was shown that the topology of the early flame kernel has a specific signature owing to its small size compared with the large turbulent scales, which can have a significant impact on the early transition to a fully turbulent flame. Since the global heat release rate is coupled to the evolution of total flame area, which is in turn related to the first two central moments of the curvature distribution (cf. (1.11)), the dynamics of flame curvature will be investigated hereafter. In § 4.1, the dependence of flame wrinkling on D_0/l_t will be assessed based on the curvature variance evolution. Run-to-run variations in the early flame front geometry of engine-relevant flame kernels will be attributed to flame/turbulence interactions by analysis of the mean curvature balance equation in § 4.2. Further, the development of flat nibs with high positive curvature at the tips shown for the engine-relevant flame kernel configuration (cf. figure 1) suggests a characteristic evolution of the third central moment (skewness) of the curvature distribution, which will be considered as a marker for characteristic flame kernel/turbulence interactions in § 4.3.

4.1. *Variance of the mean curvature distribution*

In the following, the flame front geometry evolution of all flames will be quantified by the respective curvature variance histories, which are shown in figure 4. Note that the upper x-axis indicates the size of engine kernel I. If the transition from a quasi-laminar flame kernel to a fully developed turbulent flame was governed by the high-wavenumber range of the energy spectrum characterized by an upper cutoff scale of the order of the flame diameter, one would expect the rate of variance formation to increase with D_0/l_t. By comparing the results from the planar flame, the large flame kernel and engine kernel II, this assumption seems to hold. However, engine kernel I develops curvature variance significantly faster than the large flame kernel and noticeably exceeds the variance level of engine kernel II during the early development phase.

Since the governing mechanisms of curvature production and dissipation vary in positively and negatively curved flame zones (Dopazo *et al.* 2018), both regions will be distinguished in the following analysis. For brevity, only the curvature variance conditioned on the sign of the curvature (cf. (S-2.1) in the supplementary material)

https://doi.org/10.1017/jfm.2019.995 Published online by Cambridge University Press

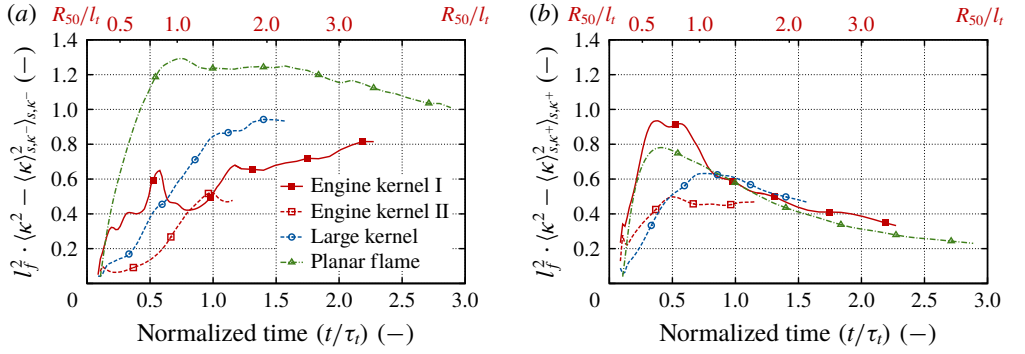


FIGURE 5. Evolution of the conditional curvature variance in regions of negative (*a*) and positive (*b*) curvature for all flames. The upper *x*-axes indicate the size of engine kernel I.

will be discussed here, while conditionally averaged curvatures are depicted in figure S-3 in the supplementary material. As shown in figure 5(*a*), the conditional variance evaluated in negatively curved regions follows similar trends as discussed for the unconditional variance. By contrast, the conditional curvature variance evaluated in positively curved regions of engine kernel I even exceeds the maximum reached for the planar flame (cf. figure 5*b*). This excess variance quickly decays to similar levels as observed in the planar flame and the large flame kernel during the time interval $(0.6\tau_t < t < 0.8\tau_t)$. Simultaneously, there is a local minimum in the conditional curvature variance in negatively curved regions of engine kernel I, which then recovers the variance level of engine kernel II. Hence, excessive curvature variance occurs in both positively and negatively curved regions. Note that the respective local maxima develop at different times. More insights into these dynamics will be provided in § 4.2 by analysis of the mean curvature transport equation. It should be noted that according to (1.11), the previously discussed decay of excessive curvature variance is responsible for a plateau in total flame area rate of change observed for engine kernel I (Falkenstein *et al.* 2019), similar to some realizations of previous two- (Thévenin *et al.* 2002) and three-dimensional flame kernel DNS (Thévenin 2005).

4.2. *Mean curvature transport*

We start from the mean curvature transport formulation for scalar iso-surfaces propagating with non-uniform displacement speed, as recently derived by Dopazo *et al.* (2018). Advection and the reaction–diffusion imbalance result in a total velocity of every scalar iso-surface element, which is given by

$$u_i^{(T)} = u_i + s_d^{(T)} n_i^{(T)}. \tag{4.1}$$

For the definition of the displacement speed $s_d^{(T)}$, refer to (1.4). The superscript denotes the scalar field used for analysis, which is the temperature in this case. In order to follow the physical analysis of curvature dynamics by Pope (1988) more closely, the equation is slightly reformulated as (cf. § A.1 for details):

$$\frac{\mathrm{D}_T(\kappa^{(T)})}{\mathrm{D}_T(t)} = \kappa^{(T)} a_n^{(T)} - 2S_{ij}^{(T)} \frac{\partial n_j^{(T)}}{\partial x_i} - \left[\frac{\partial^2 u_j^{(T)}}{\partial x_i^2} n_j - \frac{\partial^2 u_n^{(T)}}{\partial x_n^2} \right]. \tag{4.2}$$

https://doi.org/10.1017/jfm.2019.995 Published online by Cambridge University Press

The total (kinematic) strain rate tensor is given by

$$S_{ij}^{(T)} = \frac{1}{2}\left(\frac{\partial u_i^{(T)}}{\partial x_j} + \frac{\partial u_j^{(T)}}{\partial x_i}\right), \tag{4.3}$$

and the total normal strain rate is

$$a_n^{(T)} = n_i^{(T)} \frac{\partial u_i^{(T)}}{\partial x_j} n_j^{(T)} = \frac{\partial u_n^{(T)}}{\partial x_n}. \tag{4.4}$$

For brevity, the superscript will be omitted below. In order to separate effects related to the velocity field (superscript u) from those related to flame propagation (superscript p), (4.2) can be expanded as

$$\begin{aligned}\frac{\mathrm{D}_T(\kappa)}{\mathrm{D}_T(t)} = {} & \overbrace{\kappa a_n}^{\mathfrak{T}_n^u} + \overbrace{\kappa \frac{\partial s_d}{\partial x_n}}^{\mathfrak{T}_n^p} \overbrace{- 2 S_{ij} \frac{\partial n_j}{\partial x_i}}^{\mathfrak{T}_t^u} \overbrace{- 2 S_{ij}^p \frac{\partial n_j}{\partial x_i}}^{\mathfrak{T}_t^p} \\ & \underbrace{- \left[\frac{\partial^2 u_j}{\partial x_i^2} n_j - \frac{\partial^2 u_n}{\partial x_n^2}\right]}_{\mathfrak{T}_b^u} \underbrace{- \left[\frac{\partial^2 (s_d n_j)}{\partial x_i^2} n_j - \frac{\partial^2 s_d}{\partial x_n^2}\right]}_{\mathfrak{T}_b^p},\end{aligned} \tag{4.5}$$

where the flame propagation strain tensor is defined as

$$S_{ij}^p = \frac{1}{2}\left(\frac{\partial (s_d n_i)}{\partial x_j} + \frac{\partial (s_d n_j)}{\partial x_i}\right). \tag{4.6}$$

According to Pope (1988), the evolution of curvature is determined by a balance between bending and straining of the scalar iso-surface. On the right-hand side of (4.5), three main effects can be identified among the flow-field- and flame-propagation-related terms. Effects of normal strain (subscript n) due to non-uniformities of the flow and propagation velocities along the normal direction of an already curved scalar iso-surface are accounted for by $\mathfrak{T}_n^u$ and $\mathfrak{T}_n^p$. Additionally, the geometry of a surface with non-zero curvature may be altered by flow and propagation velocity gradients in the tangential plane, which is quantified by the tangential strain terms (subscript t) $\mathfrak{T}_t^u$ and $\mathfrak{T}_t^p$. The third effect is added by the terms $\mathfrak{T}_b^u$ and $\mathfrak{T}_b^p$, which consider second derivatives of the flow and propagation velocities in the iso-surface tangential directions and cause surface bending (subscript b). Among these three phenomena, bending is the only mechanism which can cause an initially planar iso-surface geometry to become wrinkled. Note that flame kernels are initialized with (possibly large) positive curvature, i.e. the $\mathfrak{T}_n^*$ and $\mathfrak{T}_t^*$ terms may significantly contribute to the curvature balance from the beginning.

For the analysis of flame curvature dynamics, all terms on the right-hand side of (4.5) have been integrated over the flame structure, but split into contributions from regions with positive and negative curvature (cf. (S-2.1) in the supplementary material). A statistical analysis on curvature dynamics in a jet flame, but using the curvature equation formulation proposed by Dopazo *et al.* (2018), has been recently carried out by Cifuentes *et al.* (2018). Note that, in the formulation (4.5), the two bending effects are related to the terms considered by Dopazo *et al.* (2018) as ($\mathfrak{T}_b^u = T_2 + T_4 + T_5$) and ($\mathfrak{T}_b^p = T_7 + T_9 + T_{10}$). As shown by Cifuentes *et al.* (2018),

https://doi.org/10.1017/jfm.2019.995 Published online by Cambridge University Press

the terms T_2 and T_4, as well as T_7 and T_9 mostly balance each other when conditioned upon the reaction progress variable.

The following discussion is focussed on the distinctive flame curvature distribution evolution of engine kernel I, characterized by the temporary occurrence of high variance (cf. figure 4). It will be shown that, due to the small initial kernel diameter and correspondingly high positive curvature, strong tangential strain may immediately amplify the curvature magnitude through stretching ($\mathfrak{T}_t^u$). By contrast, rapid production of large negative curvature magnitudes by tangential derivatives in flame displacement speed ($\mathfrak{T}_t^p$) relies on the initial formation of negatively curved flame regions by second derivatives of the velocity field through bending ($\mathfrak{T}_b^u$).

In figures 6(*a*) and 6(*b*) the histories of net curvature production in negatively and positively curved flame regions are shown for all three flame kernels. Note that the sign convention in the figures is such that positive terms describe production of curvature, i.e. the lines show the evolution of $(\sum \mathrm{sgn}(\kappa) \cdot \mathfrak{T}_*^*)$. According to the local maxima in conditional curvature variance of engine kernel I (cf. figure 5), one would expect initially excessive production of positive curvature, and slightly delayed but pronounced production of negative curvature. This is confirmed in figures 6(*b*) and 6(*a*) by comparison to the other two flame kernels. Further, it is shown that the engine-relevant flame kernel configuration exhibits strong run-to-run variations in curvature production. The physical mechanisms leading to the temporary occurrence of substantial curvature production differ between positively and negatively curved flame regions, as will be described hereafter.

In figures 6(*d*) and 6(*f*), the production of positive curvature by flow terms $\mathfrak{T}_*^u$ and flame propagation terms $\mathfrak{T}_*^p$ is depicted for both engine-relevant flame kernels. For $(t > 1.0 \cdot \tau_t)$, only minor differences between flame kernel realizations persist and the present results are in good qualitative agreement with previous studies (Cifuentes *et al.* 2018; Alqallaf, Klein & Chakraborty 2019). However, noticeable deviations between both flame kernels exist during the early development phase. From figure 6(*d*) it can be concluded that the main reason for stronger initial production of positive curvature in engine kernel I is the temporarily increased flow tangential strain term ($\mathfrak{T}_t^u$). It should be noted that this term is particularly effective, if the flame front features high positive curvature (cf. figure S-4(*a*) in the supplementary material), which is intrinsic to the engine-relevant flame kernel configuration. Further, also the dissipative net effect of flame propagation on positively curved flame regions (cf. figure 6*f*) is weaker in engine kernel I compared to II during $(0.2\tau_t < t < 0.5\tau_t)$. Note that the straining/bending balance due to flame propagation is reversed during this phase, which is a direct consequence of increased probability of high positive curvatures. As shown in previous studies (Cifuentes *et al.* 2018; Alqallaf *et al.* 2019), the curvature-conditioned means of $\mathfrak{T}_t^p$ and $\mathfrak{T}_b^p$ exhibit a saddle point at $\kappa = 0$, while both terms substantially deviate from zero only at elevated curvatures (cf. figure S-4*c*,*d*) in the supplementary material). Hence, the temporary occurrence of extreme curvatures may change the respective overall straining/bending effect in sign. Additionally, the dissipative effect of flame propagation on positively curved regions in engine kernel I is weakened by the increased level of $\mathfrak{T}_n^p$ during early flame kernel development.

Although the development of excessive curvature variance in negatively curved regions of engine kernel I is less pronounced compared to positively curved zones (cf. figure 5), noticeable differences in negative curvature production exist between both flame kernel realizations, as shown in figure 6(*c*,*e*). At late times, the production of negative curvature is governed by the flame propagation term $\mathfrak{T}_t^p$. Since the curvature-conditioned mean of this term is small at curvature radii well above the

https://doi.org/10.1017/jfm.2019.995 Published online by Cambridge University Press

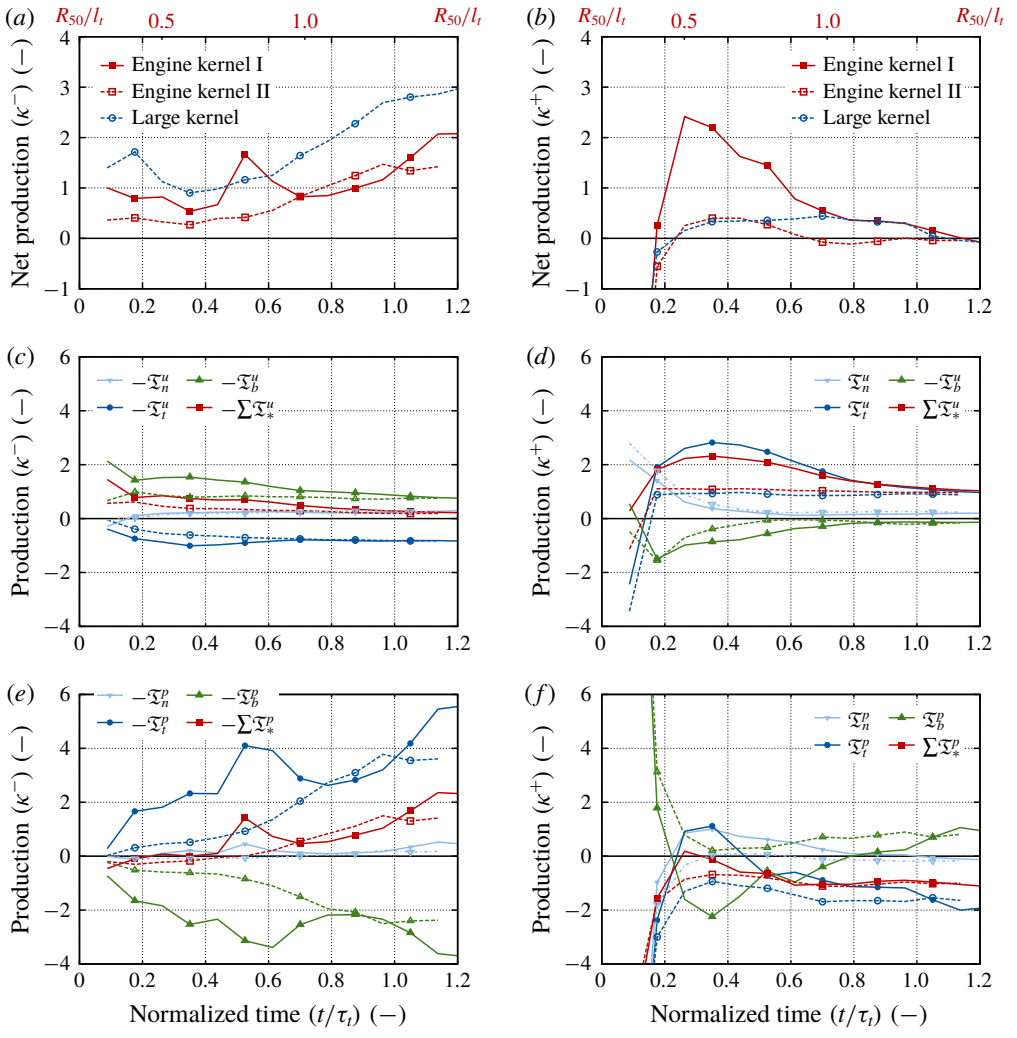


FIGURE 6. Net production terms of mean curvature (cf. right-hand side in (4.5)) for all flame kernels (*a*,*b*). Production of negative curvature by velocity field (*c*) and flame propagation (*e*) and production of positive curvature by velocity field (*d*) and flame propagation (*f*) for engine kernel I (solid lines) and engine kernel II (dashed lines). The upper *x*-axes indicate the size of engine kernel I.

laminar flame thickness (cf. figure S-4(*c*) in the supplementary material), the initial generation of negatively curved flame kernel regions may be accelerated by a different mechanism. As shown in figure 6(*c*), bending caused by second derivatives of the fluid velocity ($\mathfrak{T}_b^u$) is initially the dominant process, which is strongest in engine kernel I. Hence, the flow field is responsible for the formation of some negatively curved flame kernel regions, where the curvature magnitude is amplified by the flame propagation term $\mathfrak{T}_t^p$. Note that the combination of both effects seems to require a certain lag time, which explains the delayed local maximum in conditional variance in figure 5(*a*).

https://doi.org/10.1017/jfm.2019.995 Published online by Cambridge University Press

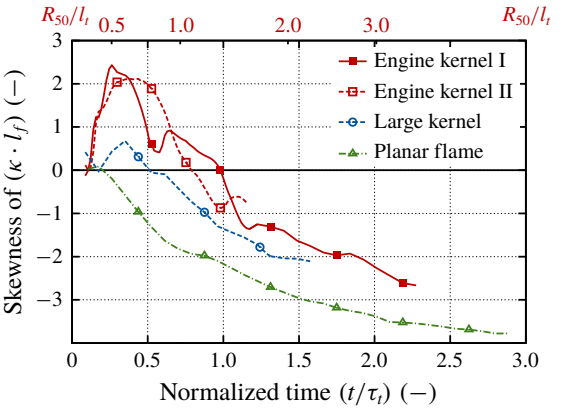


FIGURE 7. Skewness of the surface-weighted curvature distribution as a function of time.

To summarize, the analysis of mean flame curvature transport terms has shown that engine kernel I temporarily exhibits high curvature variance due to two primary effects caused by early flame kernel/flow interactions. First, high tangential strain produces excessive positive curvatures. This effect is favoured by the initially large positive curvature intrinsic to the engine-relevant flame kernel configuration, but requires certain flow conditions at the ignition location, which may vary strongly between different kernel realizations. Second, turbulent eddies cause flame front bending through second derivatives of the velocity field, which leads to initial formation of negative curvature. Moderate negative curvature magnitudes are further amplified by flame propagation, which leads to cusp formation. In the next section, it will be shown that the initial amplification of positive curvature accompanied by inhibited formation of negative curvature results in a positively skewed curvature distribution of small flame kernels, which is not observed in the other flame configurations.

4.3. *Skewness of the mean curvature distribution*

It is well known that in both laminar (Zel'dovich 1966) and weakly turbulent (Karlovitz, Denniston & Wells 1951) premixed flames, propagation of corrugated fronts causes cusp formation by Huygens' principle, leading to skewness towards negative curvatures (Shepherd & Ashurst 1992; Shepherd *et al.* 2002). In highly turbulent flows, two additional mechanisms of negatively curved cusp formation resulting from flow-induced flame collisions were proposed by Poludnenko & Oran (2011). Since the curvature skewness contains the signatures of flame propagation, thermal expansion and turbulent flame wrinkling, Creta *et al.* (2016) proposed the skewness of the curvature PDF as a marker for the occurrence of Darrieus–Landau instabilities in weakly turbulent flames. Hereafter, curvature skewness will be shown to contain the signature of characteristic flame kernel/turbulence interactions.

In figure 7, the skewness of the surface-weighted curvature distribution is depicted for each flame as a function of time. Towards the end of the simulations, the curvature distributions of all flames are indeed negatively skewed. This behaviour can be explained by the dominance of the flame propagation terms in the mean curvature balance equation, particularly $\mathfrak{T}_t^p$, which produce negative curvature (cf. figure 6*e*). With respect to flame kernel development, recall that the analysis in § 4.2 has shown that the initial amplification of high positive curvature by $\mathfrak{T}_t^u$ is a feature of the

https://doi.org/10.1017/jfm.2019.995 Published online by Cambridge University Press

engine-relevant flame kernel configuration due to flame initiation with small diameter. According to figure 1(*a*,*b*), excessive positive curvatures are generated in regions with high compressive strain, which is consistent with the negative sign of $\mathfrak{T}_t^u$ and may be further investigated by considerations in a flame tangential, local coordinate system (Cifuentes *et al.* 2018). In figure S-5 of the supplementary material, preferential alignment of the principal axes corresponding to the most positive curvature and the most compressive strain is demonstrated for both engine-relevant flame kernels. The resulting amplification of positive curvature during the early kernel development phase induces a long tail on the positive side of the curvature distribution. This effect has been observed in both engine-relevant flame kernel realizations, but to different extents. Regarding negative curvature, recall that the initial formation is caused by bending due to turbulent eddies, which induce non-zero second derivatives of the flow velocity. In figure 6(*a*) it was shown that the net production of negatively curved flame regions is weaker for the engine-relevant flame kernels compared to the large kernel. Hence, the flow scales responsible for the bending effect may not be able to effectively alter the flame surface of kernels with small size. The combination of delayed production of negatively curved and strong production of positively curved zones causes the curvature distribution of both engine kernels I and II to become noticeably skewed towards positive curvature, as shown in figure 7. Note that the delayed production of negative curvature is particularly evident for engine kernel II, while engine kernel I initially exhibits very strong production of positive curvature (cf. figure 6*a*,*b*).

In section 4 of the supplementary material, it is shown that the occurrence of strong positive skewness is not just an artefact of the present engine-relevant flame kernel realizations, but unique to the small flame kernel configuration. Hence, the curvature skewness contains information on the early flame kernel topology evolution caused by the delayed formation of negatively as opposed to positively curved regions, and most prominently, on the effect of high compressive strain leading to excessive positive curvatures. The latter effect will be related to large-scale turbulent flow motion in § 5.

5. Length-scale-dependent flame front/flow field alignment

Alignment statistics have been used by several researchers to quantify the evolution of non-reacting (Ashurst *et al.* 1987) and reacting (Chakraborty & Swaminathan 2007; Kim & Pitsch 2007) scalar fields. Local alignment between scalar gradients and strain principal axes determines normal and tangential strain rates, which in turn appear in the transport equations of scalar gradient magnitude or scalar dissipation rate, iso-surface area (cf. (1.1)) and curvature (cf. (4.5)), among others. Non-reacting scalar gradients tend to align with the most compressive strain (Ashurst *et al.* 1987), while in premixed flames, predominance of heat release induces preferential alignment with the most extensive strain as Damköhler numbers are increased (Chakraborty & Swaminathan 2007). In this work, alignment statistics for all principal strain components have been computed and related to data from the literature (cf. figure S-7 in the supplementary material), while the following discussion will be limited to the most compressive principal strain for brevity. Evidence will be provided for the dominant role of large-scale turbulent flow structures in changing the volumetric flame topology of early, engine-relevant flame kernels.

Recall that in § 3.1 it has been shown that significant differences exist in the very early topological development of the small and large flame kernels, which is reflected in the evolution of curvature skewness, as discussed in § 4.3. Since the only

https://doi.org/10.1017/jfm.2019.995 Published online by Cambridge University Press

difference between the two flame kernel configurations is the length-scale ratio D_0/l_t, it is hypothesized that the nature of early flame/turbulence interactions is significantly different in both cases. In particular, it is assumed that the engine-relevant flame kernel is initially governed by large-scale flow structures that change the overall flame topology, while the large flame kernel is subject to flame front wrinkling by flow scales which are mostly smaller than the flame size. Hence, the objective of the present analysis is to quantify the length-scale dependence of flame front orientation with respect to the velocity field. To achieve this, small-scale velocity fluctuations were removed from the flow field by applying a low-pass filter. If early flame kernel/turbulence interactions were governed by large-scale flow structures, preferential alignment of the flame front normal vectors with the principal axes of the strain tensor evaluated from the filtered as opposed to the unfiltered velocity field would be expected. Since the focus of this analysis is on length scales of at least the same order as the flame kernel size, the filtered velocity field has been obtained by applying a box filter of size ($\Delta = 0.5 \cdot l_t$), which is approximately equal to a characteristic radius of the small flame kernels at ($t = 0.25 \cdot \tau_t$). This analysis is to some extent similar to a study on scale dependence of enstrophy production by Buxton, Laizet & Ganapathisubramani (2011). In that study, statistics of angles between vorticity and strain tensor eigenvectors were calculated from velocity fields filtered at different scales and compared to analyse scale dependence.

In figure 8, PDFs of the cosines of the angle between the flame normal vectors and the most compressive principal strain axes are plotted for all flame kernels at ($t = 0.25 \cdot \tau_t$) and ($t = 1.0 \cdot \tau_t$). Note that normal vectors have been computed from temperature gradients throughout the flame structure, without conditioning on a particular iso-surface. On the right-hand side of figure 8 it is shown that flame normals eventually align with the most compressive strain in all three flame kernels. Further, removing small flow scales from the velocity field by applying a low-pass filter only has a moderate effect on the alignment statistics at ($t = 1.0 \cdot \tau_t$). By contrast, the preferential flame front alignment with the large flow scales for engine kernel I is much more pronounced at ($t = 0.25 \cdot \tau_t$), as shown in figure 8(*a*). In line with the initially high positive curvature production by strain (cf. figure 6*d*) and the strong deformation of the overall flame topology (cf. figure 3), the flame front alignment statistics of engine kernel I exhibit the strongest length-scale dependence among all three flame kernels. Although preferential alignment with the large flow scales is also observed in engine kernel II at this early time instant, the PDF is much less affected by the low-pass filtering than in case of engine kernel I. Note that the length-scale dependence may vary significantly in magnitude over time, but the discussed qualitative differences between both small flame kernel realizations were found throughout the early development phase. In contrast to the engine-relevant flame kernels, the large flame kernel does not exhibit preferential flame front alignment with large-scale flow structures at both shown times, as expected.

To conclude the analysis of early flame kernel/turbulence interactions, it has been shown that the small flame kernel is subject to strong compressive strain caused by turbulent eddies that are at least as large as the flame radius. As a result, the young flame becomes strongly distorted, though a coherent kernel structure is maintained under the present conditions. Since these effects are highly dependent on the local flow conditions, significant run-to-run variations in curvature variance may occur, which affect the evolution of total flame area through (1.11). The observed large-scale-dominated early flame/turbulence interactions rapidly generate burned

https://doi.org/10.1017/jfm.2019.995 Published online by Cambridge University Press

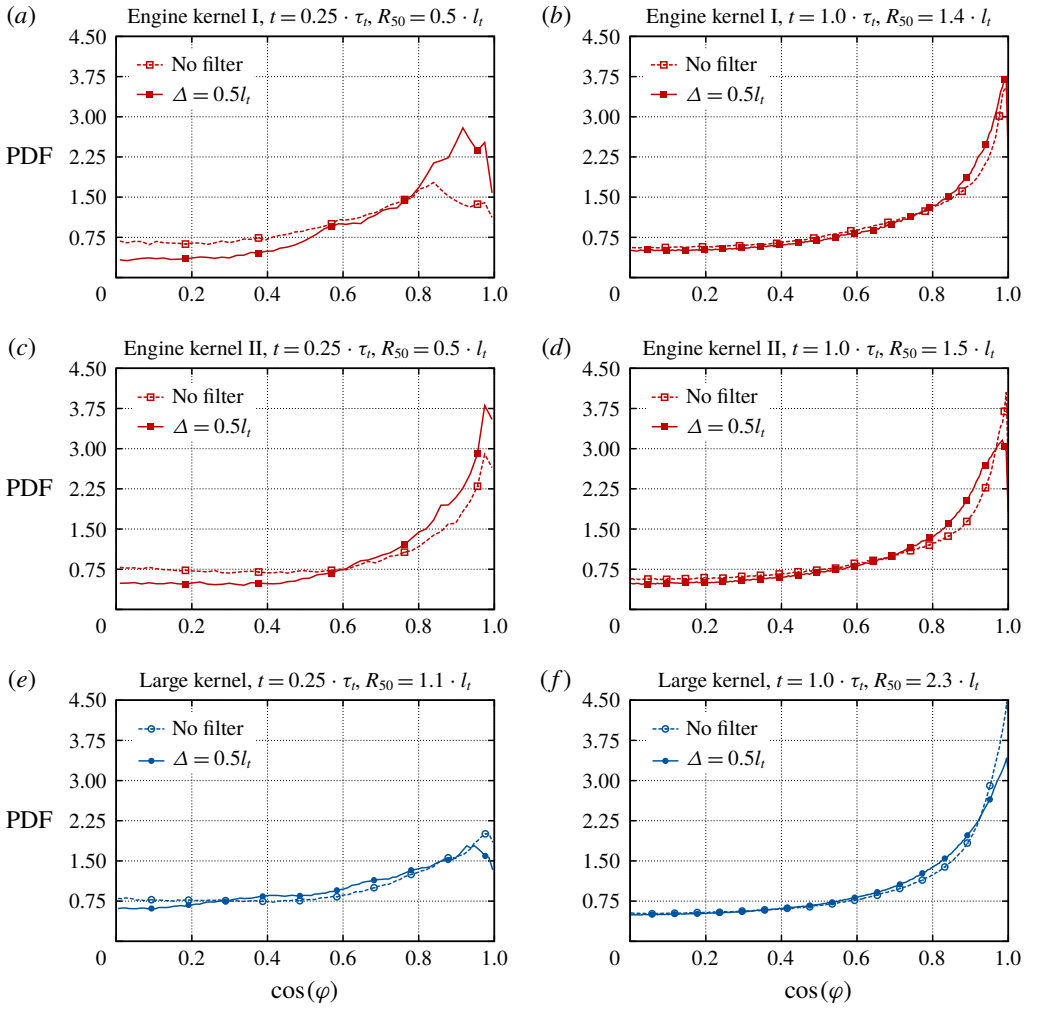


FIGURE 8. Alignment of the flame front normal vectors with the principal axes of the most compressive strain for engine kernel I (*a*,*b*), engine kernel II (*c*,*d*) and the large flame kernel (*e*,*f*) at ($t = 0.25 \cdot \tau_t$) and ($t = 1.0 \cdot \tau_t$).

regions of flat shape, which feature high positive curvatures caused by tangential strain. Consequently, the curvature PDF of the small flame kernels is inversely skewed for ($t \lesssim 1.0 \cdot \tau_t$). In other words, the early flame kernel is subject to local strain caused by turbulent length scales larger than the flame size, which leads to a production of small curvature radii. This process is in some sense similar to scalar turbulence with $Sc > 1$, where small scalar structures (large gradients) in a range between the Kolmogorov and the Batchelor scale ($\eta_B < l < \eta$) are produced by strain at larger length scales ($l > \eta$) (Batchelor 1959). Different from this statistical effect in scalar mixing, the dominance of flame curvature production by strain due to local, large-scale flow motion is reduced as the flame grows in size and flame/turbulence interaction approaches statistical behaviour.

https://doi.org/10.1017/jfm.2019.995 Published online by Cambridge University Press

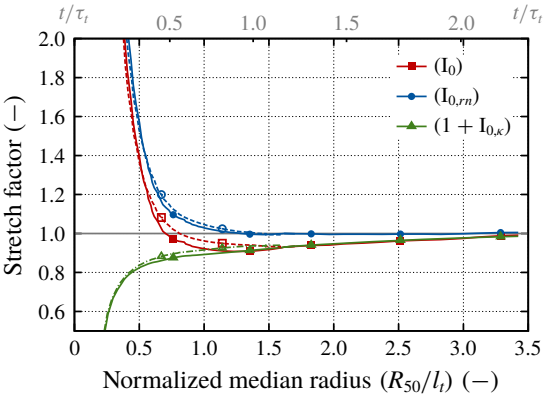


FIGURE 9. Flame displacement speed deviation from a laminar unstretched flame as function of flame kernel size for engine kernel I (solid lines) and engine kernel II (dashed lines).

6. Relevance and implications for engine combustion and modelling

From laser-optical engine experiments it was found that even when misfires occur, a small flame kernel is initiated by spark ignition (Peterson *et al.* 2011), which rapidly expands and interacts with the flow. However, ignition kernels may be affected by turbulence even before the critical radius for self-sustaining flame propagation is reached. The effect of high-temperature ignition pocket stretching by turbulence was identified by Castela *et al.* (2016) in a DNS study on plasma-assisted combustion using a sophisticated ignition model. In a recent DNS study, Uranakara *et al.* (2017) observed global flame kernel extinction within less than one laminar flame time. Hence, interactions of the early ignition or flame kernel with the flow field can be expected to play an important role, even when the young flame is still affected by the spark. In the present work, the ignition heat source is meant to represent the macroscopic spark effect, which accelerates the early flame kernel growth as shown in figure 9 by the global stretch factor ($\bar{I}_0 = \bar{I}_{0,rn} + \bar{I}_{0,\kappa}$) plotted as a function of flame kernel radius. The time evolution of all three stretch factor components has been discussed in our previous study (Falkenstein *et al.* 2019). Here, it should be noted that flame propagation is very consistent with experimental observations by Herweg & Maly (1992), who found that the minimum burning velocity of the young flame occurs at a flame radius of approximately one integral length scale. In the present study, interactions of large-scale turbulent flow structures with the flame kernel topology were identified as a characteristic mechanism of early flame kernel development, which occurs while the flame is still affected by the initial ignition energy supply ($\bar{I}_0 < 2$). Possible interactions between severe flame kernel distortion and the development of a self-sustaining flame structure from a high-temperature ignition pocket are aspects suggested for future investigations on kernel extinction.

The results of the present study have several practical implications, since one of the key challenges in SI engine development is the reduction of cycle-to-cycle variations (Young 1981; Fansler & Wagner 2015), which are thought to be strongly dependent on early flame kernel development. More recently, simulations of stochastic phenomena in engines have become feasible by using the large-eddy simulation (LES) technique (Rutland 2011; Hasse 2016). However, computation of a series of engine cycles introduces the need for modelling spark ignition and early flame kernel development,

https://doi.org/10.1017/jfm.2019.995 Published online by Cambridge University Press

since the associated time and length scales are very small. As a consequence, the ability of a simulation framework to predict cycle-to-cycle variations is particularly dependent on the accuracy of the early flame kernel model. Under the conditions investigated in the present work, run-to-run variations were identified which may need to be captured by predictive models. It has been shown that large-scale turbulent flow structures can lead to strong topology changes of the young flame, which may substantially alter early kernel growth due to preferential diffusion effects present in common transportation fuel/air mixtures ($Le_{eff} \approx 2$), or to cause global extinction by flame kernel breakup in extreme cases. This effect of large-scale flow structures is in contrast to the assumption of kernel wrinkling by a successively wider range of turbulent length scales, which implies that initially only small flow scales are important (Herweg & Maly 1992; Echekki *et al.* 1994). In LES, information on large flow structures is naturally available since these are resolved on the computational grid. In order to capture interactions with the small flame, Eulerian flame kernel models were proposed by Richard *et al.* (2007) and Colin & Truffin (2011). However, these models can only reproduce early distortion of the flame as observed in the present study, if the young kernel shape is resolved on the computational grid when the flame diameter is smaller than the integral length scale ($O(2$ mm) in engines). Since the flame kernel grows rapidly in size, this can be achieved by temporary mesh refinement as long as ($t \lesssim 0.5 \cdot \tau_t$). For rigorous model testing, a DNS database of several flame realizations computed up to ($t = 1.0 \cdot \tau_t$) would be sufficient according to the present results.

7. Conclusions

Since cycle-to-cycle variations in SI engines are correlated with the very early combustion phase, a better understanding of the governing effects during turbulent flame kernel development is desirable. In this work, characteristic topological changes intrinsic to the engine-relevant flame kernel configuration have been identified and attributed to flame interactions with large-scale turbulent flow structures, which cause noticeable run-to-run variations. Specifically, analyses of flame front geometry evolution in three flame configurations with different D_0/l_t have shown the following.

(i) The global curvature variance during flame development does not follow a clear trend for small D_0/l_t, but varies significantly between different flame kernel realizations.

(ii) Although sometimes used as modelling assumption, the development of curvature variance or flame wrinkling does not seem to be restricted by an upper cutoff scale of the order of the kernel size.

(iii) In some realizations of the engine-relevant flame kernel configuration, excessive curvature variance is produced during the initial kernel development phase.

(iv) The decay of this excess variance causes a plateau in net flame surface area production (Falkenstein *et al.* 2019), which can be explained by (1.11).

The physical origin of the stochastic occurrence of high curvature variance has been further investigated based on the mean curvature transport equation, which enabled the following conclusions:

(i) Curvature evolution in both positively and negatively curved flame regions is substantially influenced by the local flow conditions, which leads to pronounced run-to-run variations.

https://doi.org/10.1017/jfm.2019.995 Published online by Cambridge University Press

(ii) The small initial kernel diameter and correspondingly high positive curvature intrinsic to the engine-relevant flame kernel configuration favours the immediate amplification of positive curvature by tangential strain.
(iii) This initial curvature production by flow straining may lead to a long tail on the positive side of the curvature distribution.
(iv) By contrast, production of large negative curvature magnitudes by tangential derivatives in flame displacement speed relies on the initial formation of negatively curved flame regions by turbulent eddies, which induce non-zero second derivatives of the fluid velocity (bending). Compared to other flame configurations, this effect is less effective in case of small flame kernels, possibly due to the small flame diameter respective of the relevant flow scales.
(v) Consequently, the curvature distribution of small flame kernels becomes strongly skewed towards positive curvatures, which is the opposite of what is observed for developed flames.

Further, the impact of flame kernel initiation with smaller diameter than the energy-containing turbulent length scales has been examined, which is a characteristic feature of SI engine combustion. The analysis of length-scale-dependent flame front alignment with the flow field has shown the following.

(i) At early times ($t \approx 0.25 \cdot \tau_t$), flame normal vectors are preferentially aligned with the most compressive principal axis of the strain tensor computed from a low-pass filtered velocity field, where flow scales up to the kernel size have been removed.
(ii) Consequently, the small flame kernel is subject to compressive strain caused by turbulent eddies that are at least as large as the flame radius, i.e. the mean flame front curvature radius and the governing flow scales are of similar order.
(iii) This characteristic flame kernel/turbulence interaction has a strong impact on the volumetric flame topology and flame front geometry, and distinguishes early flame kernel development from the evolution of a statistically planar flame brush.

It is hypothesized that the demonstrated flame kernel distortion by large-scale turbulent flow structures is a major contributor to cycle-to-cycle variations in engines and may even result in global extinction under extreme conditions. In the presence of preferential diffusion effects, flame response to high stretch caused by strain and topology changes might be severe, and will be investigated in the future.

In the present work, only two flame realizations were considered. Hence, conclusions on the impact of fluctuations in early flame kernel growth on heat release at later times or on cycle-to-cycle variations in engines could not be drawn. Still, characteristic observations from the small flame kernel datasets were confirmed in local regions of the other flames to ensure the validity of the conclusions on early flame kernel/flow interactions.

Acknowledgements

The authors from RWTH Aachen University gratefully acknowledge partial funding by Honda R&D and by the Deutsche Forschungsgemeinschaft (DFG, German Research Foundation) under Germany's Excellence Strategy – Exzellenzcluster 2186 'The Fuel Science Centre' ID: 390919832. The authors gratefully acknowledge the Gauss Centre for Supercomputing e.V. (www.gauss-centre.eu) for funding this project by providing computing time on the GCS Supercomputer Super-MUC at Leibniz Supercomputing Centre (LRZ, www.lrz.de). Data analyses were performed with

https://doi.org/10.1017/jfm.2019.995 Published online by Cambridge University Press

computing resources granted by RWTH Aachen University under project thes0373. S.K. gratefully acknowledges financial support from the National Research Foundation of Korea (NRF) grant by the Korea government (MSIP) (no. 2017R1A2B3008273).

Declaration of interests

The authors report no conflict of interest.

Supplementary material

Supplementary material is available at https://doi.org/10.1017/jfm.2019.995.

Appendix A

A.1. *Derivation of the mean curvature transport equation*

In order to derive the form of the mean curvature evolution equation used in this study (cf. (4.2)), we formulate equation (38) from the study of Dopazo *et al.* (2018) in the present notation,

$$\frac{\mathrm{D}_\vartheta(\kappa^{(\vartheta)})}{\mathrm{D}_\vartheta(t)} = \kappa^{(\vartheta)} a_n^{(\vartheta)} + \frac{\partial a_n^{(\vartheta)}}{\partial x_n} - 2S_{ij}^{(\vartheta)} \frac{\partial n_j^{(\vartheta)}}{\partial x_i} - \frac{\partial S_{ij}^{(\vartheta)}}{\partial x_i} n_j^{(\vartheta)} + \frac{\partial W_{ij}^{(\vartheta)}}{\partial x_i} n_j^{(\vartheta)}, \tag{A 1}$$

where ϑ refers to the scalar field used to define iso-surfaces. The velocity of an iso-surface element is given by,

$$u_i^{(\vartheta)} = u_i + s_d^{(\vartheta)} n_i^{(\vartheta)}. \tag{A 2}$$

For the definitions of the normal vector $n_i^{(\vartheta)}$ and displacement speed $s_d^{(\vartheta)}$, refer to (1.3) and (1.4). The scalar iso-surface described in the moving reference frame is subject to the total normal strain rate,

$$a_n^{(\vartheta)} = n_i^{(\vartheta)} \frac{\partial u_i^{(\vartheta)}}{\partial x_j} n_j^{(\vartheta)} = \frac{\partial u_n^{(\vartheta)}}{\partial x_n}, \tag{A 3}$$

and the total strain rate and rotation rate tensors are defined as,

$$S_{ij}^{(\vartheta)} = \frac{1}{2}\left(\frac{\partial u_i^{(\vartheta)}}{\partial x_j} + \frac{\partial u_j^{(\vartheta)}}{\partial x_i}\right), \tag{A 4}$$

$$W_{ij}^{(\vartheta)} = \frac{1}{2}\left(\frac{\partial u_i^{(\vartheta)}}{\partial x_j} - \frac{\partial u_j^{(\vartheta)}}{\partial x_i}\right). \tag{A 5}$$

To rewrite (A 1) in terms of second derivatives of the total velocity, we use

$$-S_{ij}^{(\vartheta)} + W_{ij}^{(\vartheta)} = -\frac{\partial u_j^{(\vartheta)}}{\partial x_i} \tag{A 6}$$

to combine the last two terms on the right-hand side of (A 1). The second term on the right-hand side is modified by using the normal strain definition (cf. (A 3)) to obtain:

$$\frac{\mathrm{D}_\vartheta(\kappa^{(\vartheta)})}{\mathrm{D}_\vartheta(t)} = \kappa^{(\vartheta)} a_n^{(\vartheta)} - 2S_{ij}^{(\vartheta)} \frac{\partial n_j^{(\vartheta)}}{\partial x_i} - \left[\frac{\partial^2 u_j^{(\vartheta)}}{\partial x_i^2} n_j^{(\vartheta)} - \frac{\partial^2 u_n^{(\vartheta)}}{\partial x_n^2}\right], \tag{A 7}$$

https://doi.org/10.1017/jfm.2019.995 Published online by Cambridge University Press

which is equivalent to (4.2). The first two terms on the right-hand side describe the effects of normal and tangential strain on curvature evolution, respectively. The last two terms in brackets are responsible for iso-surface bending by second derivatives of the total velocity in the tangential plane (Pope 1988).

REFERENCES

ABDEL-GAYED, R. G., AL-KHISHALI, K. J. & BRADLEY, D. 1984 Turbulent burning velocities and flame straining in explosions. *Proc. R. Soc. Lond.* A **391** (1801), 393–414.

AKINDELE, O., BRADLEY, D., MAK, P. & MCMAHON, M. 1982 Spark ignition of turbulent gases. *Combust. Flame* **47**, 129–155.

ALEIFERIS, P., TAYLOR, A., ISHII, K. & URATA, Y. 2004 The nature of early flame development in a lean-burn stratified-charge spark-ignition engine. *Combust. Flame* **136** (3), 283–302.

ALQALLAF, A., KLEIN, M. & CHAKRABORTY, N. 2019 Effects of Lewis number on the evolution of curvature in spherically expanding turbulent premixed flames. *Fluids* **4** (1), 12.

ASHURST, W. T., KERSTEIN, A. R., KERR, R. M. & GIBSON, C. H. 1987 Alignment of vorticity and scalar gradient with strain rate in simulated Navier–Stokes turbulence. *Phys. Fluids* **30** (8), 2343–2353.

BATCHELOR, G. K. 1959 Small-scale variation of convected quantities like temperature in turbulent fluid Part 1. General discussion and the case of small conductivity. *J. Fluid Mech.* **5** (1), 113–133.

BODE, J., SCHORR, J., KRÜGER, C., DREIZLER, A. & BÖHM, B. 2017 Influence of three-dimensional in-cylinder flows on cycle-to-cycle variations in a fired stratified DISI engine measured by time-resolved dual-plane PIV. *Proc. Combust. Inst.* **36** (3), 3477–3485.

BOGER, M., VEYNANTE, D., BOUGHANEM, H. & TROUVÉ, A. 1998 Direct numerical simulation analysis of flame surface density concept for large eddy simulation of turbulent premixed combustion. *Symp. (Intl) Combust.* **27** (1), 917–925.

BRADLEY, D., LAWES, M., SCOTT, M. & MUSHI, E. 1994 Afterburning in spherical premixed turbulent explosions. *Combust. Flame* **99** (3), 581–590.

BRADLEY, D. & LUNG, F.-K. 1987 Spark ignition and the early stages of turbulent flame propagation. *Combust. Flame* **69** (1), 71–93.

BUSCHBECK, M., BITTNER, N., HALFMANN, T. & ARNDT, S. 2012 Dependence of combustion dynamics in a gasoline engine upon the in-cylinder flow field, determined by high-speed PIV. *Exp. Fluids* **53** (6), 1701–1712.

BUXTON, O. R. H., LAIZET, S. & GANAPATHISUBRAMANI, B. 2011 The interaction between strain-rate and rotation in shear flow turbulence from inertial range to dissipative length scales. *Phys. Fluids* **23** (6), 061704.

CANDEL, S. M. & POINSOT, T. J. 1990 Flame stretch and the balance equation for the flame area. *Combust. Sci. Technol.* **70** (1–3), 1–15.

CASTELA, M., FIORINA, B., COUSSEMENT, A., GICQUEL, O., DARABIHA, N. & LAUX, C. O. 2016 Modelling the impact of non-equilibrium discharges on reactive mixtures for simulations of plasma-assisted ignition in turbulent flows. *Combust. Flame* **166**, 133–147.

CHAKRABORTY, N. & SWAMINATHAN, N. 2007 Influence of the Damköhler number on turbulence-scalar interaction in premixed flames. I. Physical insight. *Phys. Fluids* **19** (4), 045103.

CIFUENTES, L., DOPAZO, C., SANDEEP, A., CHAKRABORTY, N. & KEMPF, A. 2018 Analysis of flame curvature evolution in a turbulent premixed bluff body burner. *Phys. Fluids* **30** (9), 095101.

COLIN, O. & TRUFFIN, K. 2011 A spark ignition model for large eddy simulation based on an FSD transport equation (ISSIM-LES). *Proc. Combust. Inst.* **33** (2), 3097–3104.

CRETA, F., LAMIONI, R., LAPENNA, P. E. & TROIANI, G. 2016 Interplay of Darrieus–Landau instability and weak turbulence in premixed flame propagation. *Phys. Rev.* E **94**, 053102.

DAMKÖHLER, G. 1940 Der Einfluss der Turbulenz auf die Flammengeschwindigkeit in Gasgemischen. *Z. Elektrochem.* **46** (11), 601–626.

https://doi.org/10.1017/jfm.2019.995 Published online by Cambridge University Press

DOPAZO, C., MARTIN, J., CIFUENTES, L. & HIERRO, J. 2018 Strain, rotation and curvature of non-material propagating iso-scalar surfaces in homogeneous turbulence. *Flow Turbul. Combust.* **101** (1), 1–32.

ECHEKKI, T. & CHEN, J. 1999 Analysis of the contribution of curvature to premixed flame propagation. *Combust. Flame* **118**, 308–311.

ECHEKKI, T. & KOLERA-GOKULA, H. 2007 A regime diagram for premixed flame kernel-vortex interactions. *Phys. Fluids* **19** (4), 043604.

ECHEKKI, T., POINSOT, T., BARITAUD, T. & TROUVÉ, A. 1994 Modeling and simulation of turbulent flame kernel evolution. *Tech. Rep.* 41525. Institut Français du Pétrole.

FALKENSTEIN, T., KANG, S., CAI, L., BODE, M. & PITSCH, H. 2019 DNS study of the global heat release rate during early flame kernel development under engine conditions. *Combust. Flame*, Preprint, arXiv:1908.07556 (accepted).

FANSLER, T. D. & WAGNER, R. M. 2015 Cyclic dispersion in engine combustion – introduction by the special issue editors. *Intl J. Engine Res.* **16** (3), 255–259.

GASHI, S., HULT, J., JENKINS, K. W., CHAKRABORTY, N., CANT, S. & KAMINSKI, C. F. 2005 Curvature and wrinkling of premixed flame kernels comparisons of oh plif and DNS data. *Proc. Combust. Inst.* **30** (1), 809–817.

HAQ, M., SHEPPARD, C., WOOLLEY, R., GREENHALGH, D. & LOCKETT, R. 2002 Wrinkling and curvature of laminar and turbulent premixed flames. *Combust. Flame* **131** (1), 1–15.

HASSE, C. 2016 Scale-resolving simulations in engine combustion process design based on a systematic approach for model development. *Intl J. Engine Res.* **17** (1), 44–62.

HEIM, D. & GHANDHI, J. 2011 A detailed study of in-cylinder flow and turbulence using PIV. *SAE Intl J. Engines* **4** (1), 1642–1668.

HERWEG, R. & MALY, R. R. 1992 A fundamental model for flame kernel formation in SI engines. In *International Fuels Lubricants Meeting Exposition*. SAE International.

HESSE, H., CHAKRABORTY, N. & MASTORAKOS, E. 2009 The effects of the Lewis number of the fuel on the displacement speed of edge flames in igniting turbulent mixing layers. *Proc. Combust. Inst.* **32** (1), 1399–1407.

HEYWOOD, J. 1994 Combustion and its modeling in spark-ignition engines. In *Proceedings of the Third International Symposium on Diagnostics and Modeling of Combustion in Internal Combustion Engines (COMODIA), Yokohama, Japan, July 11–14*, pp. 1–15.

HIRSCHFELDER, J. O., CURTISS, C. F. & BIRD, R. B. 1954 *Molecular Theory of Gases and Liquids*. Wiley.

JUNG, D., SASAKI, K. & IIDA, N. 2017 Effects of increased spark discharge energy and enhanced in-cylinder turbulence level on lean limits and cycle-to-cycle variations of combustion for SI engine operation. *Appl. Energy* **205**, 1467–1477.

KARLOVITZ, B., DENNISTON, D. W. & WELLS, F. E. 1951 Investigation of turbulent flames. *J. Chem. Phys.* **19** (5), 541–547.

KIM, S. H. & PITSCH, H. 2007 Scalar gradient and small-scale structure in turbulent premixed combustion. *Phys. Fluids* **19** (11), 115104.

LUCA, S., ATTILI, A., SCHIAVO, E. L., CRETA, F. & BISETTI, F. 2019 On the statistics of flame stretch in turbulent premixed jet flames in the thin reaction zone regime at varying Reynolds number. *Proc. Combust. Inst.* **37** (2), 2451–2459.

MENEVEAU, C. & POINSOT, T. 1991 Stretching and quenching of flamelets in premixed turbulent combustion. *Combust. Flame* **86** (4), 311–332.

MÜLLER, B. 1998 Low-Mach-number asymptotics of the Navier–Stokes equations. *J. Engng Maths* **34** (1), 97–109.

PETERS, N. 1992 A spectral closure for premixed turbulent combustion in the flamelet regime. *J. Fluid Mech.* **242**, 611–629.

PETERS, N. 1999 The turbulent burning velocity for large-scale and small-scale turbulence. *J. Fluid Mech.* **384**, 107–132.

PETERSON, B., REUSS, D. L. & SICK, V. 2011 High-speed imaging analysis of misfires in a spray-guided direct injection engine. *Proc. Combust. Inst.* **33** (2), 3089–3096.

https://doi.org/10.1017/jfm.2019.995 Published online by Cambridge University Press

PETERSON, B., REUSS, D. L. & SICK, V. 2014 On the ignition and flame development in a spray-guided direct-injection spark-ignition engine. *Combust. Flame* **161** (1), 240–255.

PITSCH, H. & PETERS, N. 1996 Numerical and asymptotic studies of the structure of premixed iso-octane flames. *Symp. (Intl) Combust.* **26** (1), 763–771.

POLUDNENKO, A. & ORAN, E. 2011 The interaction of high-speed turbulence with flames: turbulent flame speed. *Combust. Flame* **158** (2), 301–326.

POPE, S. B. 1988 The evolution of surfaces in turbulence. *Intl J. Engng Sci.* **26**, 445–469.

REDDY, H. & ABRAHAM, J. 2013 Influence of turbulence-kernel interactions on flame development in lean methane/air mixtures under natural gas-fueled engine conditions. *Fuel* **103**, 1090–1105.

RICHARD, S., COLIN, O., VERMOREL, O., BENKENIDA, A., ANGELBERGER, C. & VEYNANTE, D. 2007 Towards large eddy simulation of combustion in spark ignition engines. *Proc. Combust. Inst.* **31** (2), 3059–3066.

RUTLAND, C. J. 2011 Large-eddy simulations for internal combustion engines – a review. *Intl J. Engine Res.* **12** (5), 421–451.

SCHIFFMANN, P., REUSS, D. L. & SICK, V. 2018 Empirical investigation of spark-ignited flame-initiation cycle-to-cycle variability in a homogeneous charge reciprocating engine. *Intl J. Engine Res.* **19** (5), 491–508.

SCURLOCK, A. & GROVER, J. 1953 Propagation of turbulent flames. *Symp. (Intl) Combust.* **4** (1), 645–658.

SHEPHERD, I. & ASHURST, W. 1992 Flame front geometry in premixed turbulent flames. *Symp. (Intl) Combust.* **24** (1), 485–491.

SHEPHERD, I., CHENG, R., PLESSING, T., KORTSCHIK, C. & PETERS, N. 2002 Premixed flame front structure in intense turbulence. *Proc. Combust. Inst.* **29** (2), 1833–1840.

SUBRAMANIAN, V., DOMINGO, P. & VERVISCH, L. 2009 Turbulent flame spreading mechanisms after spark ignition. *AIP Conf. Proc.* **1190** (1), 68–89.

THÉVENIN, D. 2005 Three-dimensional direct simulations and structure of expanding turbulent methane flames. *Proc. Combust. Inst.* **30** (1), 629–637.

THÉVENIN, D., GICQUEL, O., CHARENTENAY, J. D., HILBERT, R. & VEYNANTE, D. 2002 Two- versus three-dimensional direct simulations of turbulent methane flame kernels using realistic chemistry. *Proc. Combust. Inst.* **29** (2), 2031–2039.

URANAKARA, H. A., CHAUDHURI, S. & LAKSHMISHA, K. 2017 On the extinction of igniting kernels in near-isotropic turbulence. *Proc. Combust. Inst.* **36** (2), 1793–1800.

VASUDEO, N., ECHEKKI, T., DAY, M. S. & BELL, J. B. 2010 The regime diagram for premixed flame kernel-vortex interactions – revisited. *Phys. Fluids* **22** (4), 043602.

WANG, H., HAWKES, E. R., CHEN, J. H., ZHOU, B., LI, Z. & ALDÉN, M. 2017*a* Direct numerical simulations of a high Karlovitz number laboratory premixed jet flame – an analysis of flame stretch and flame thickening. *J. Fluid Mech.* **815**, 511–536.

WANG, Z., LIU, H. & REITZ, R. D. 2017*b* Knocking combustion in spark-ignition engines. *Progr. Energy Combust. Sci.* **61**, 78–112.

WENZEL, H. & PETERS, N. 2000 Direct numerical simulation and modeling of kinematic restoration, dissipation and gas expansion effects of premixed flames in homogeneous turbulence. *Combust. Sci. Technol.* **158** (1), 273–297.

YOUNG, M. B. 1981 Cyclic dispersion in the homogeneous-charge spark-ignition engine – a literature survey. *SAE Trans.* **90**, 49–73.

ZEL'DOVICH, Y. B. 1966 An effect which stabilizes the curved front of a laminar flame. *J. Appl. Mech. Techn. Phys.* **7** (1), 68–69.

ZENG, W., KEUM, S., KUO, T.-W. & SICK, V. 2019 Role of large scale flow features on cycle-to-cycle variations of spark-ignited flame-initiation and its transition to turbulent combustion. *Proc. Combust. Inst.* **37** (4), 4945–4953.

https://doi.org/10.1017/jfm.2019.995 Published online by Cambridge University Press